

Stay Tuned: Tuning Actuation Force in Functional Objects

Athina Panopoulou

atpa@di.ku.dk

Department of Computer Science, University of Copenhagen
Copenhagen, Denmark

Valkyrie Savage

vasa@di.ku.dk

Department of Computer Science, University of Copenhagen
Copenhagen, Denmark

Atul Chaudhary

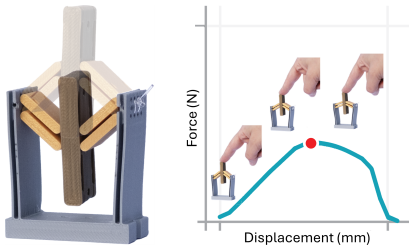
atch@di.ku.dk

Department of Computer Science, University of Copenhagen
Copenhagen, Denmark

Daniel Ashbrook

dan@di.ku.dk

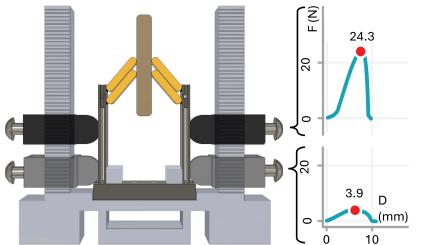
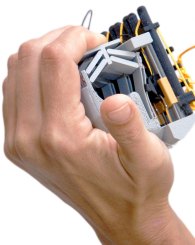
Department of Computer Science, University of Copenhagen
Copenhagen, Denmark



(a) Bistable design and function



(b) Scalable in size



(c) Tunable actuation force

Figure 1: Our bistable mechanism offers varying force resistance at different displacements (a). It can be scaled up or down to meet various applications' size and force requirements and is fabricated using low-cost 3D printers (b). Post-fabrication, its actuation force (red dot) can be tuned further (c).

Abstract

The physical properties of objects cannot typically be adjusted post-fabrication to meet specific needs or preferences. While 3D printing offers the potential of design-time customization, manipulating object properties after the object has been printed remains challenging. We present a 3D printable bistable mechanism with an actuation force that can be quickly and repeatedly adjusted after fabrication by up to a factor of 5.25, enabling tunable monostable or bistable behavior. Our mechanism, printable on commodity low-cost 3D printers, incorporates off-the-shelf elastic threads to maintain robust operation when fabricated at different sizes. We present an evaluation of how manipulating geometric parameters influences the post-print behavior of our design and demonstrate its versatility in five functional objects.

CCS Concepts

- Human-centered computing → Haptic devices;
- Applied computing → Computer-aided manufacturing.

Keywords

3D-printing, threads, tunable mechanisms, tactile devices, reconfigurable metamaterials, reconfigurable properties

ACM Reference Format:

Athina Panopoulou, Atul Chaudhary, Valkyrie Savage, and Daniel Ashbrook. 2025. Stay Tuned: Tuning Actuation Force in Functional Objects. In *Designing Interactive Systems Conference (DIS '25), July 5–9, 2025, Funchal, Portugal*. ACM, New York, NY, USA, 18 pages. <https://doi.org/10.1145/3715336.3735804>

1 Introduction

Functional objects need to adjust to specific needs and preferences when used by different people, for different purposes, or at different times. For example, a mechanical keyboard's actuation force might benefit from being adjustable uniformly based on personal preferences, per-key for specific applications, or variably over time as health conditions change muscle strength. However, more often than not, mass-produced functional objects cannot be adjusted post-manufacture, leading to unmet needs or preferences, increased material consumption and waste, and lower usability.

In contrast to mass production, the rise of reliable low-cost 3D printers offers the potential to fabricate personalized functional objects. A large body of research in this area has explored design-time customization of object properties, such as color [41], translucency [32], mass [31], moment of inertia [13], force response [2], strength [29], and deformation [26]. While such design-time decisions enable broad customizability, once such objects are printed,



This work is licensed under a Creative Commons Attribution-NonCommercial 4.0 International License.

DIS '25, July 05 – July 09, 2025, Funchal, Portugal

© 2025 Copyright held by the owner/author(s).

ACM ISBN 978-1-4503-XXXX-X/18/06

<https://doi.org/10.1145/3715336.3735804>

their properties are fixed. To address this limitation, another branch of research has investigated how to manipulate passive object properties *post-fabrication*, such as visual appearance [21], texture [18], or elasticity [48]. Quickly tuning the passive force-response of 3D printed objects over a wide force range, however, remains challenging due to the rigidity of typical printable materials such as PLA and the complexity of the tuning process.

Our work addresses these challenges by incorporating elastic threads into a 3D printed bistable mechanism (Fig. 1(a)), adding a high degree of flexibility and robustness to the design’s moving parts. The inclusion of threads also enables our mechanism to be scaled in size with no significant design changes, from centimeter- to decimeter-scale (Fig. 1(b)). We call each individual instance of this mechanism a *cell*. Our cells’ tuning method takes advantage of the strength of the threads, allowing the actuation force of a printed model to be adjusted in a wide range (Fig. 1(c)). To understand how decisions made at design time influence the behavior of the fabricated cells, we evaluate the impact on actuation force of three mechanisms, six geometric parameters, and post-fabrication tuning. These results inform a physics-based model of our mechanism, enabling designers to determine appropriate geometric parameter values for a given application.

We illustrate the versatility of our design via five applications ranging from finger to body scale, which demonstrate: continuous and discrete tuning; high actuation-force tuning between 43–226 N in a single cell; scaling of tunable cells in sizes ranging between 15–186 mm; both selective single-cell and simultaneous multi-cell tuning in multi-mechanism arrangements; and design-time-configurable mono- or bistable behavior.

In summary, we contribute the following:

- a novel mechanism with on-the-spot tunable actuation force which is manufacturable using low-cost 3D printers and threads
- a characterization of the design of the mechanism to fulfill various application requirements (scalability and complexity), as well as strategies and designs for coordinated tuning in complex multi-cell arrangements
- five example objects ranging from hand- to body-scale, which highlight the design’s adaptability in various application requirements, as well as its tuning versatility and varied capabilities.

2 Related Work

2.1 Passive Force-Feedback

Although passive functional devices by definition supply no energy themselves, only dissipating energy provided by the user [14], they are nonetheless remarkably effective. Many of the passive functional devices we interact with in everyday life—for example, electrical switches, elevator buttons, doors, and stereo knobs—offer mechanisms which provide passive force feedforward and feedback. Feedforward suggests what action to expect when we initiate an interaction [45]: a light switch provides minimal resistance when we start to toggle it. Feedback indicates what action took place when we end an interaction: a button-press provides a *click* when pressed.

In this vein, researchers [4] have explored multiple techniques to enable passive force-feedback in fabricated objects that provide informative interactions when functioning. Several projects use magnets to provide customizable force-feedback for printed [52], knitted [30], or sheet-based [49] objects. Another common approach closely related to our work involves the careful design of compliant structures and the selection of suitable materials for their construction. Carefully designed compliant structures can act as springs providing variability in resistance [12], and can also deliver detent [28] and bounce feedback [53]. Compliant structures can also provide bistability: a familiar “switch-flip” sensation of initial resistance followed by “snap-through”. Materials used in compliant designs include ABS or PLA printer filament [19], a combination of fabric and printed plastic [11], and PET plastic sheets [6].

Each of these approaches enables the specification of an object’s haptic properties, which remain fixed post-fabrication. The actuation force of printed springs [12] is influenced by the material compliance [11] as well as the geometry of the spring design [15]. Similarly, detent [28] or resistance feedback [53] are introduced as geometric features during the design process. However, some applications could benefit if the force-responsive properties of device could be adjusted *post-fabrication*; for example, force feedback for surgery simulation [7], interaction with virtual objects [40], or per-button actuation force customizability per-button in keyboards [38] all depend on the object’s response to user force being variable rather than “baked in” at fabrication time.

One line of research explores reconfigurable discrete force resistance levels set at design time. Kuppens et al. [25] designed a bistable mechanism that could be switched between two actuation force levels. Other researchers have explored cell assemblies to provide finer-grained post-fabrication reconfiguration. Yang et al. [48] developed a grid of spring and damper cells, each of which could be selectively activated via a printed configuration layer, allowing the grid’s overall force response to be tuned. Jiang et al. [20] demonstrated a tiled haptic floor where 2×2 groups of tiles could be toggled between two different levels to provide locally varying resistance.

Tuning haptic properties on a continuous scale has also been explored. Some printable materials soften when heated, allowing the behavior of printed materials to be tuned post-fabrication [44, 51], but the materials must cool before a different tuning can be selected. Research in metamaterial design has built structures to smoothly transition between two textures [18], allowing real-time tuning. Metamaterial cells have also been used to control stiffness via pneumatic inflation [43] or magnetic actuation [9]; however, these approaches require complex fabrication processes. In a similar line of research, we focus on tuning the actuation force post-fabrication to specific force levels within continuous ranges using a bistable mechanism as the cell.

To tune our mechanism, we modify one of its geometric parameter values post-fabrication, inspired by an approach of Stapel and Herder [42]. In their work, they reconfigure the stiffness of a compliant slider-rocker mechanism. Similar to their work, our bistable mechanism allows for continuous tuning between two force levels, which can vary by a factor of up to $\times 5.25$. To allow convenient integration of the mechanism in the prototyping of functional objects of

various sizes, we explore how modifying its geometric parameters affects the actuation force.

Few prior works have investigated varying the size of post-fabrication tunable haptic mechanisms. While some research in mechanical metamaterials has explored the effects of adding multiple copies of the same-sized cell [46], the only research we are aware of involving scaling the design of an *individual* tunable cell or mechanism is that of Jiang et al. [20] reported scaling their cell design between 3–6.5 cm to achieve larger motion; however, details on how the actuation force changed were not provided.

2.2 Bistable Mechanisms

As discussed above, multiple methods for fabricating passive force-feedback devices have been demonstrated in the literature. One common approach is to use a bistable mechanism to provide controllable motion [20] and resistance to force [25]. Bistable mechanisms have two stable positions where their energy is minimized, making them “want” to stay in one of those positions. Between the two stable positions is an unstable equilibrium position, where the mechanism is under equal forces from both sides but requires very little energy to be snapped towards a stable position. A familiar example of a bistable mechanism is a light switch, which stays in the “on” or “off” position by itself, and snaps to one of those positions if placed somewhere in-between: it is possible but challenging to “balance” it in the exact middle. Bistable mechanisms can be implemented in multiple ways, including with hinges [50] or buckling elements [47].

Many 3D printable bistable-mechanism designs use buckling, relying on the compliance of the printable material to operate [19, 20, 25]. A drawback of this approach, however, is that when the mechanism is moved to just at its halfway point, where it will “snap through” to a new stable position, the materials experience significant stress [54], which can lead to material fatigue, i.e., increased flexibility or even breaking [17, p. 17]. Alternate materials such as rubber [43] or metallic glass [54] offer high strength-to-flexibility ratios, but are not accessible outside of industrial or specialized lab environments.

Our passive force-feedback mechanism adapts previous compliant bistable designs [8, 34] for accessible manufacturing with commodity fused-filament fabrication (FFF) 3D printers, using the most common filament type, PLA. To overcome problems of material fatigue and fracture, we replace some high-stress areas of the compliant design with fiber-based hinges (Figure 3); although we hand-thread the fibers to assemble our prototypes, modified low-cost 3D printers could potentially fabricate the entire mechanism without human intervention [3]. Aside from increasing robustness, our fiber-based hinges also enable our design to be easily scaled; in contrast, compliant hinges can become too small to print when scaled down [25].

3 Design Approach

We designed our mechanism to fulfill several goals. To allow broad use of our design, our cells must be easily *fabricable* on commodity equipment, such as low-cost 3D printers. Cells should also be *scalable*: the same basic design and tuning mechanisms should work at multiple physical sizes, from hand-scale to body-scale, and be

operable under varying force requirements. Cells should be easily *tunable* after fabrication: we want to be able to adjust the actuation force of a cell within some application-appropriate range. Finally, we want to be able to tune our cells either individually or in groups when they are *incorporated* in complex multi-cell arrangements.

Our bistable design is inspired by existing compliant bistable mechanism designs [19, 35, 36, 39]. A typical cell design (Figure 2) consists of multiple flexible *beams* (compliant structures) linked by a rigid *shuttle*, with the ends of the beams connected to a rigid *frame*. Force is applied to the shuttle (Figure 1(a)). As the beams are moved downward out of the first stable position, they become more and more compressed until they pass the midpoint, at which point they release their stored energy to “snap through” into the second stable position [35]. We define the actuation force as the maximum force required to move the shuttle from the first to the second stable position (red dot in Figure 1(a)).

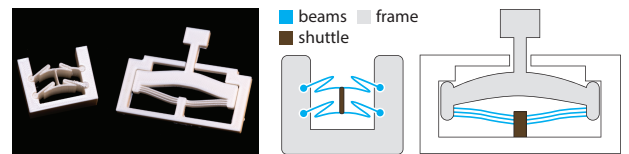


Figure 2: Many bistable cells cannot be tuned post-fabrication (left). Their function depends on flexible beams connected by a rigid shuttle in a rigid frame (right). Designs from Ion et al. [19] and Kuppens et al. [25].

Because this typical design relies on beam compliance for bistability, a balance must be struck between the amount of deflection possible, the elasticity of the material, and the actuation force of the mechanism. Materials commonly used in commodity 3D printers, such as PLA, are typically not very elastic; that is, after a small amount of deformation, they cannot return to their original shape, and may fracture or break entirely. These factors make it difficult to meet design goals; for example, a mechanism combining high actuation force with large displacement would likely break if 3D printed using PLA based on this design.

To enable a wider range of design parameters, especially the ability to achieve high actuation force and displacement, we modify this typical design. Our adaptation (Figure 3) introduces compliance in a different way and enables post-fabrication actuation force adjustment.

In our design, it is the frame and the threads rather than the beams that provide compliance to the system. We link the two compliant sides of the frame, which we now term *arms*, to a rigid *base*. This allows for post-fabrication force tuning. Additionally, we replace the compliant beams from the original design with rigid *flippers*, connected via hinges made of threads to the central rigid shuttle and the arms. During actuation, the arms now flex outwards around the connections, rather than the beams compressing to fit the space between the arms as in the original design. The use of flexible threads instead of printed material as the hinges enhances the robustness of our design. In contrast to common thermoplastic materials such as PLA, threads can be bent thousands of times without losing their flexibility or breaking. The use of threads also allows

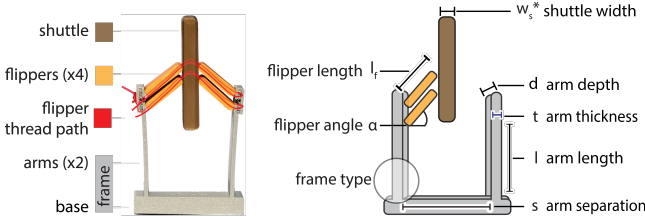


Figure 3: Our mechanism consists of five parts: the base, arms, flippers, shuttle, and threads. The threads internally connect the flippers to the arms and shuttle. We modify various geometric parameters of the mechanism, except for the one marked with an asterisk (*).

large flipper angles, and thereby greater displacement between the two stable states.

3.1 Bistable Mechanism Designs

Our new cell design offers multiple geometric parameters which can be manipulated in order to influence its actuation force (Figure 3). Most parameter values are defined pre-fabrication, while post-fabrication tuning results from varying the value of a single parameter. Conceptually, pre-fabrication tuning determines the *base actuation force* of a cell. Post-fabrication tuning modifies the module’s actuation force within a range set by its fabricated form. Base actuation force can be set based on the application requirements (e.g., a chair needs a higher base actuation force than a button does), while tuning parameters can be tweaked for current personal preference (e.g., Mama Bear prefers a softer chair than Papa Bear). Tuning can only increase the actuation force: the minimum is set by the model geometry pre-fabrication.

In addition to the geometric design parameters, we also experimented with the source of arm-base joint compliance, which affects the base force and the distribution of stress. We tested two options for the base-to-arm connection: using *flexures* as arms, or having threaded *hinges* to join the arms and the base. This results in two monolithic frame designs when using a single (uniform frame type) or multiple (flexure frame type) flexures, and a hinged design where a separate arm is connected to the base via threads (thread frame type) (Figure 4, (a)-(c)). In the thread frame, the stress in the arms is insignificant, while in the uniform and flexure frames, stress accumulates in the arms (Figure 4, bottom row (a)-(c)). Additionally, the three frame types affect the actuation force of the mechanism differently when adjusting geometric parameters of the model. We observe that monolithic designs can be used to tune the base actuation force at various levels, whereas thread-based designs cover a small range of base forces for a given thread type. Designs using solid connections locate compliance in both the connecting area and through the length of the arm itself, while compliance in hinged connections results from the stretching of the thread as the arm rotates around the connection point.

Compliance can also be distributed symmetrically or asymmetrically. Symmetrical compliance comes, naturally, from identical arms and connection types on each side, while asymmetric compliance arises when the arms are not identical: for example, if one arm is thicker and rigid, while the other has a hinge or flexures.

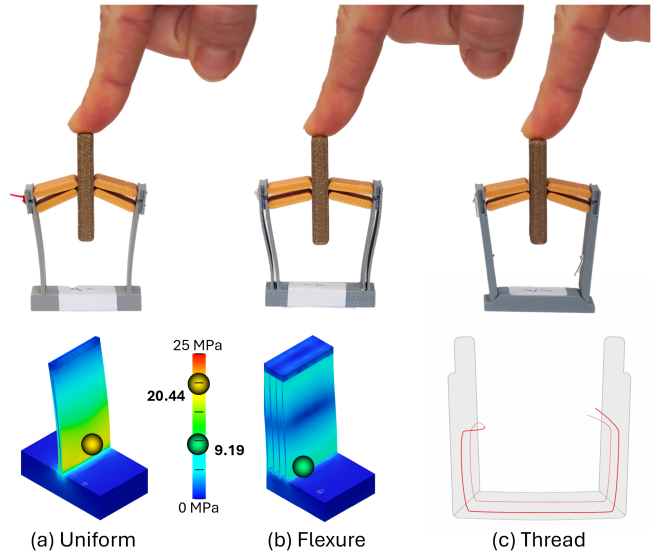


Figure 4: Sources of frame compliance: uniform arms (a), flexure arms (b), and hinged arm/base joints with threaded joints (c): each behaves differently when actuated (top). Finite element analysis in Autodesk Fusion (Appendix A) of the uniform and flexure arms shows stresses distributed similarly (bottom). The hinged arms require a thread path to function.

Asymmetrically tuned designs (illustrated in our applications in Figure 16 (a), (d), and (g)) are less complex, as the tuning mechanism only needs to work on a single arm; in addition, with one arm held rigid, space needs to be made for the flexing of only a single arm. However, their force and motion trajectory modeling is more complex than that of symmetric ones.

In addition to the above design parameters, we can also change the behavior of a cell from bi-stable to mono-stable by preventing snap-through. One approach is to modify the geometry of the shuttle so that it collides with the frame before the flippers reach the horizontal unstable equilibrium position. Another approach is restricting the outward flexing of the arms to prevent the flippers from being placed horizontally.

3.2 Mechanisms for Tuning

While design choices detailed in the previous section determine the base actuation force of the mechanism, we further developed a method to quickly and repeatedly tune a mechanism’s actuation force post-fabrication. We insert a sliding blocking component (blocker) between the outside of the arms and a more rigid structure (tuning frame) (Figure 5). Moving the blocker away from the base reduces the distance through which the arm can flex, i.e., the effective arm length, and thereby increases its actuation force. However, this is only true for monolithic frames (uniform and flexure frames). The hinges in the thread frame are not blocked by the blocker; instead, the blocker serves as the movable fulcrum of a lever created by the arms.

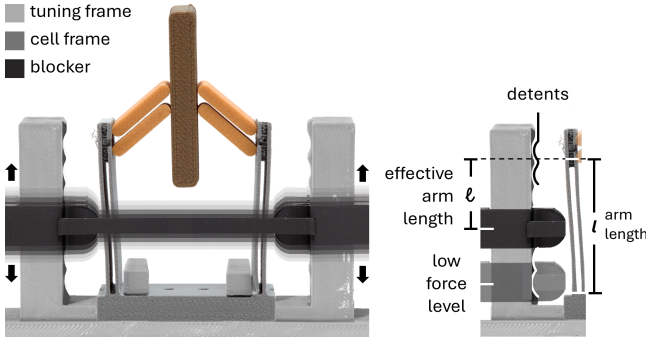


Figure 5: Effective arm length can be modified by using a blocker that slides up and down next to the mechanism’s arms, only allowing them to flex from the point where it contacts them. Adding detents to the blocker track can settle it in discrete locations and force levels, or it can be positioned continuously.

It is also possible to tune multiple mechanisms simultaneously or selectively within a multi-cell arrangement. We developed three methods to adjust blockers within cells arranged in a row: two that use threads to adjust cells either uniformly or selectively, and one that uses rigid selectors to adjust cells selectively via mechanical logic gates. The thread-based tuning approaches work well with complex or irregular objects. Threads occupy little space and easily route around corners. However, these designs do not scale well with an increasing number of cells. As the number of cells controlled by a thread increases, friction makes the thread difficult to move. In contrast, the rigid-based tuning approach, using sliders, enables addressing cells individually or on a row-by-row basis for arrangements with more cells in a row, but this method does not apply directly in designs that do not form a grid.

One approach uses threads through the tuning mechanisms, allowing us to simultaneously tune all of the cells in a row to the same resistance, or to selectively tune individual cells. By running a thread between all cells in a row and connecting it to their blockers, we can pull it to one side to simultaneously increase all cells’ force resistance, and to the other side to decrease all cells’ force resistance (Section 3.2 shows this method in the context of our chair application; see Section 6.4). We can also use a thread approach to tune individual cells. Adding a third component, a selector bead for each cell and a corresponding thread, and adding two threads in opposite paths in the tuning mechanism allows us to individually set force levels for cells. The first tuning thread (Figure 7(a)blue) moves all blockers at the highest level. The selector thread (Figure 7(b)yellow) is moved so that the corresponding selector bead is locked into a specific position. When the second tuning thread (Figure 7(c)red) is pulled, individual cells move within the range set by the bead. Figure 7(d) shows this in the context of our grip-trainer application (Section 6.1).

Another method of tuning multiple cells is via rigid mechanisms, rather than thread-based ones, specifically, by employing sliders. Figure 8 illustrates rigid tuners in conjunction with a row-column addressing mechanism inspired by an early mechanical computer [37] and based in part on an open-source design [24].

Rigidly coupling the cells’ blockers together via sliders allows multiple cells in a row to be simultaneously tuned: each square’s force response is tuned by moving the position of a sliding blocker (blue cylinder in Figure 8(a)–(d)): as the blocker moves away from the base, it restricts the flexing of the arm, which in turn increases the actuation force of the corresponding cell.

3.3 Fabrication

All of our prototypes are fabricated in PLA on Bambu Carbon X1 printers, with the following settings: 220 °C, 0.4 mm nozzle, 0.2 mm layer height, and 100 % concentric infill. Although nylon (≈ 0.49 GPa[55]) or ABS (≈ 1.1 GPa) might exhibit better elasticity, we selected PLA (≈ 3.5 GPa¹) due to its popularity, accessibility, and easy printability. All parts are fabricated laying flat on the printbed, such that layers are continuous between the arms and base (i.e., layers are U-shaped). To resolve inaccuracies in fabricated flipper angle, for the printable flipper model length we subtract 0.2 mm. We also avoid placing printing seams near the lower part of the arm and the arm-base connection areas, as they can affect functionality.

A design consideration is selecting a thread that contributes to the desired haptic effect of the functional device. Using inelastic durable threads can simplify modeling of the mechanism’s behavior, and is suitable for both high- and low-actuation-force cells. However, the use of inelastic threads results in an abrupt haptic transition between the two stable positions. For a smoother, springy haptic experience, we use elastic threads and manually pre-stretch them in similar stretch amounts.

The thickness, along with the amount of the thread stretch, affects the functionality of the mechanism. In low-actuation-force cells, using thicker or highly stretched threads can reduce the distance between the two stable positions by pre-deflecting the arms away from their rest position, bringing them closer to the unstable equilibrium and thereby modifying the actuation force. Conversely, in high-actuation-force cells, thinner threads increase the risk that the mechanism fails to switch between stable states and instead continues to slide as the threads extend.

After experimenting with a wide variety of thread materials, we settled on elastic thread sourced online under the description “0.8 mm elastic TPU clear thread”², but we were unable to obtain any detailed information about its material composition. While for the majority of our applications the diameter 0.8 mm thread works well, for low-force finger applications such as the chess board, we scale down our design and use a smaller thread size (0.6 mm), while for applications bigger in size such as the plant house and the chair application, we scale up both our mechanisms and thread (1.75 mm) to obtain the desired actuation force. For modeling, we manually stretched the thread to approximately 72% of its original length. Since this process is manual, it is inaccurate with lengths approximated within cm. For the high-force application designs, we could not provide additional manual stretching; the hand-applied force was not sufficient to stretch them; instead, the threads were just positioned in place. The selection and the placement of the inelastic thread was direct, we used a thread sourced online under

¹The PLA and ABS numbers are based on <https://static.igem.org/mediawiki/2015/2/24/CamJIC-Specs-Strength.pdf>, but can vary based on specific print setup.

²example source: <https://www.amazon.de/dp/B09KTVMYT3>

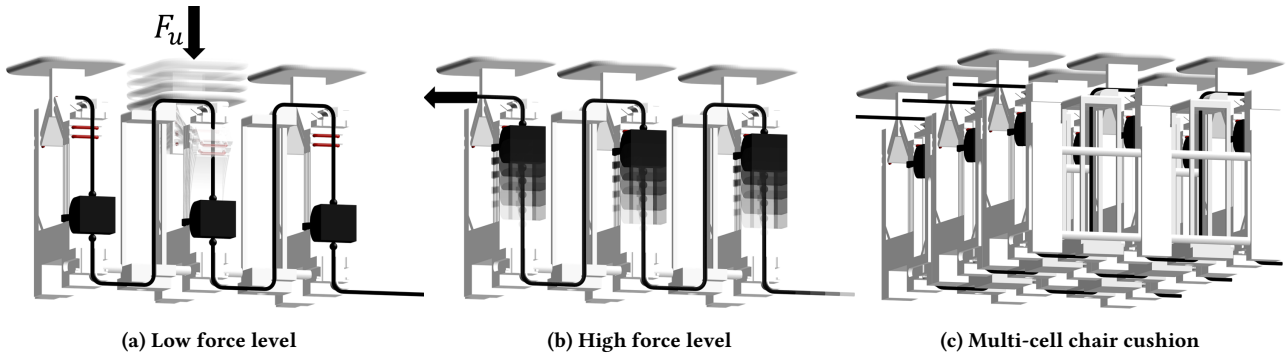


Figure 6: With tuning blockers(black) at their lowest position, applied force on the cells from a user meets low resistance (a). Pulling the tuning threads to the left raises the blockers of all cells in the row simultaneously, stiffening the user’s feeling (b). Our cushion has three rows of three pads; each row can be independently tuned using this approach (c).

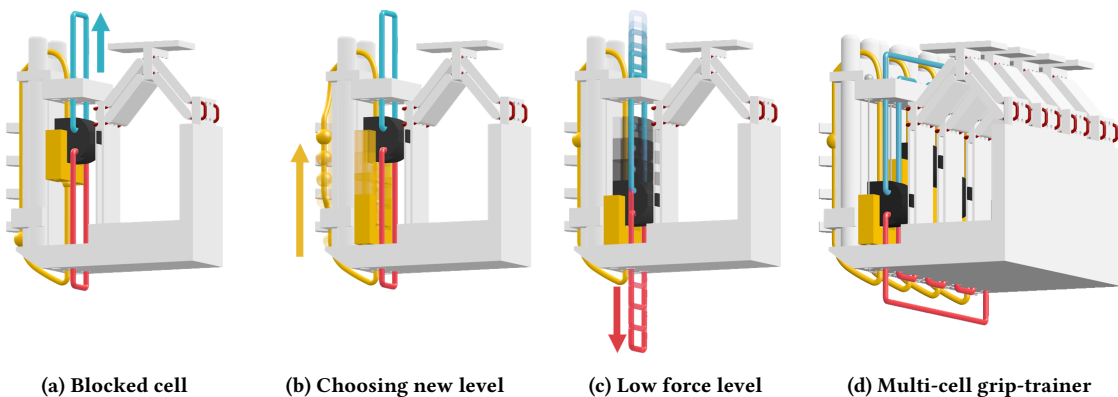


Figure 7: Per-cell thread-based tuning. The blocker(black) is raised via the top tuning thread(blue) so that the mechanism is blocked (a). To lower the force level, the selector(yellow bead) is raised into a higher restraining notch via the selector thread(yellow) (b). Finally, the lower tuning thread(red) is pulled down to move the blocker into a new level force (c). Our grip trainer has four cells that allow the cells' resistance to be adjusted simultaneously using this approach (d).

the description “0.8 mm Flat Waxed Thread”³. The thread paths used are not unique. Future work could focus on the effect of thread path on the cell functionality.

Fabrication Guidance. Figure 9 illustrates how we assemble the printed mechanism. With elastic threads, we pre-stretch the thread to approximately 72% of the total thread path length (determined via temporarily inserting an inelastic thread, marking it, then removing and measuring) as shown in 9. To add heavier or reconfigure the stretch in the flipper threads, we have used knots that connect the two thread endpoints, such as variations of the surgeon and barrel knots. The inelastic threads were loosely attached to avoid motion restriction and an increase in force. Although we manually thread mechanisms after printing, a general-purpose thread-embedding printer such as Rhapso [3] could be used in the future for fully automatic fabrication. An in-between approach is to pause the 3D printer midway through the construction of the thread paths and insert the threads before printing continues.

4 Technical Evaluation

We explore how to tune the actuation force both pre- and post-fabrication by modeling and experimentally testing the effects of geometry modifications. For our pre-fabrication exploration, we model our uniform and flexure frames as pseudo-rigid bodies and compare these theoretical results to experimental ones gathered through a lab study. We also provide experimental data on our hinged frames. These results can help designers determine how and through what range base actuation force can be adjusted. For our post-fabrication analysis, investigate tuning to understand to what extent an already fabricated mechanism's actuation force can be modified. We conduct a second lab study and fit models to the collected data, which can help designers understand how to place blockers to achieve perceptually distinct or target force levels.

4.1 Experimental Protocol

We use identical setups for the two sets of experiments reported below, where we mount fabricated mechanisms in a custom setup designed to gather force-displacement curves.

³example source: <https://www.amazon.de/dp/B0BCHP9S36>

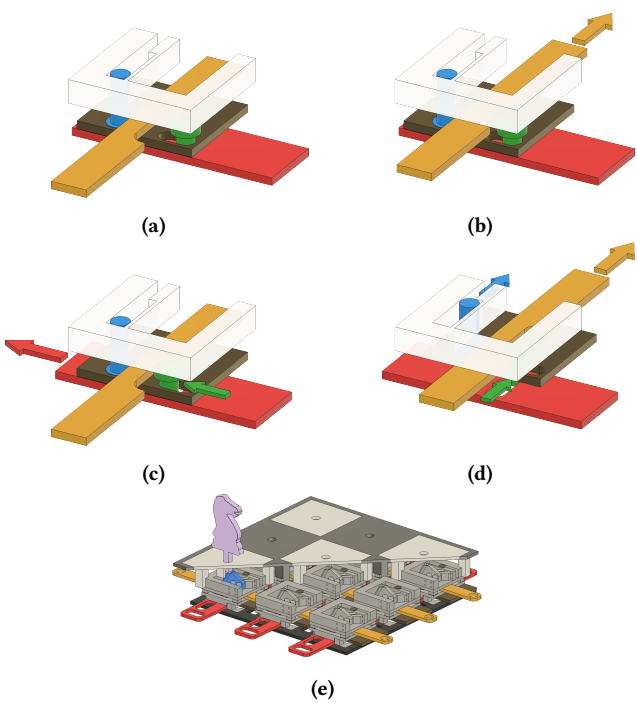


Figure 8: Simplified illustration of a single element of a row/column chainable tuning mechanism. For clarity, the shuttle, flippers, and supporting structures are not shown. (a) The blocking pin (blue) is at the bottom, and the selection pin (green) is not engaged; thus, when the tuning slider (yellow) is moved (b) the blocking pin remains in place. When the selection slider (red) is moved (c), the selection pin engages. (d) Now the tuning slider pulls the selection pin, which in turn moves the tuning plate and the blocking pin, increasing the resistance of the mechanism. (e) shows a cutaway of a 3×3 chess board. Tuning of each row can be enabled or disabled via the selection sliders, and each column is tuned via the tuning sliders.

We use an off-the-shelf push/pull force meter (BAOSHISHAN ZP-50N) with 0.1 N accuracy and 50 N maximum force mounted to a modified Creality Ender 3 Pro 3D printer (see Figure 10). Our custom software continually reads force values from the meter's serial port and controls the Z-axis of the printer to perform pushing. The system moves the Z-axis in 0.5 mm increments, pushing down on the shuttle from the upper stable position until the mechanism passes the snap-through point and transitions to the lower stable position. We repeat this procedure five times for each model, align recordings, and plot min, max, and average values. We focus here on positive *pushing* forces only: as users are not affixed to our mechanisms during snap-through, they will not experience below-zero *pulling* force.

4.2 Pre-fabrication Tuning

The values of the model's geometric parameters determine the base actuation force. For the monolithic frame types, we model these

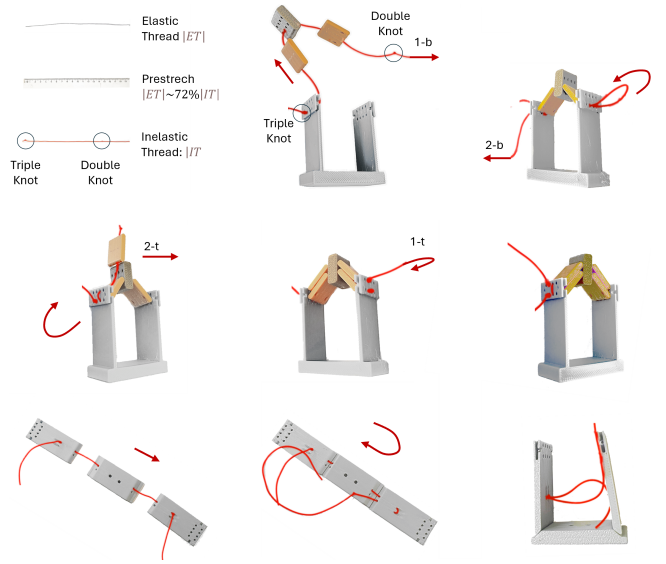


Figure 9: Fabrication involves manual assembly. It begins with the use of inelastic or elastic thread. Pre-stretching of elastic threads can be applied. Knots are placed at pre-defined distances. Threading of the first thread path in the bottom flipper series (1-b), followed by threading of the second thread path in the bottom flipper series (2-b). Next, the second (2-b) and then the first (1-b) thread path of the top flipper series are threaded. In the case of the thread frame type, a similar approach can be followed to thread the base to the arms (bottom row).

Parameter	Default value	Variants
Symmetry	Symmetric	Asymmetric
Flipper angle (α)	45°	35° or 40°
Arm length (l)	32 mm	22 mm or 62 mm
In-plane arm thickness (t)	32 mm	27 mm or 62 mm
Uniform		
Flexures		
Thread		
Out-of-plane arm depth (d)	1.6 mm	0.8 mm or 2.0 mm
Uniform	2 flexures	3 or 4 flexures
Flexures		
Thread	1 thread	2 or 3 threads
Uniform		
Flexures		
Thread		
Base in-plane width	18 mm	5 mm or 9 mm
Shuttle in-plane thickness	18 mm	5 mm or 9 mm
Shuttle out-of-plane depth	2 threads	10 or 20 threads
Asymmetric rigid arm in-plane thickness	30 mm	22 mm or 38 mm
No of Arms	2	
<hr/>		
Non-varied value		
Flipper in-plane thickness	3 mm	
Flipper out-of-plane depth	12 mm	
Base in-plane width	6 mm	
Shuttle in-plane thickness	6 mm	
Shuttle out-of-plane depth	12 mm	
Asymmetric rigid arm in-plane thickness	6 mm	
No of Arms	2	

Table 1: Default configuration for mechanism parameters used in evaluation. The top half of the table shows parameters that we varied during testing, while the bottom half shows those we held constant.



Figure 10: Our force-displacement test rig is built on a modified Creality Ender 3 Pro 3D printer and an off-the-shelf push/pull force meter.

forces using prototypes with inelastic threads as described in the Appendix. Next, we display experimental forces for models with elastic threads along with the modeled values. For the thread frame type, we only display experimental results, where we observe small force differences between different model variations.

4.2.1 Modeling. We use physics-based modeling to simulate design behavior. In particular, we seek to find the maximum force required to snap the mechanism from one stable position to the other (i.e., the actuation force) and the force profile of an actuation. We discuss the model for the Uniform frame type. Full expansion of equations is available in the Appendix as well as modifications for asymmetric and flexure designs (Appendix B).

When we consider a user pushing downwards on the shuttle, their generated force is transmitted through the flippers into the arms, deflecting them out of their fabricated position. The actuation force can be calculated at a given arm deflection and relates to fabricated geometric and material parameters (Equations (1)–(3) in the Appendix). To give an intuition behind these for design, the actuation force is expected to be proportional to the Young's modulus⁴ E of the material, the arm depth d , and the cube of arm's in-plane thickness t , and inversely proportional to a power of the arm length l . Or differently, by increasing the arm depth, one can increase the actuation force, but less drastically compared to increasing the arm thickness or decreasing the arm length.

Extension to flexure frame type. To extend to the flexure frame type, we consider the forces of several coupled flexures together in our calculation. However, the deflected beams in flexure and uniform models take different physical shapes, with the uniform model creating a filleted corner while the flexure model creates an S-like shape, something that indicates differences between the two designs (Figure 4).

Our calculations are based on the quantilever beam theory [42] and the pseudo-rigid-body model applied to each flexure or uniform arm [16, 17]. The model approximates compliant mechanisms as rigid bodies, enabling the estimation of the actuation force. The pseudo-rigid-body model is not relevant to the hinge frame type, as its arms behave as true rigid bodies with a thread-based spring hinge connecting them to the base. The reaction force coming from

⁴Roughly, how stretchy a material is.

the arm is related to the elasticity and stretching of the threads, rather than deformation of the printed bodies, a trend reflected in our results, which show a limited range of achievable forces.

4.2.2 Experiments. To inform the model, we fabricated 12 variations of the uniform and 12 variations of the flexure “default” configuration using inelastic threads and followed the approach described in the Appendix. We systematically varied them from the default configuration to collect experimental evidence for our physics-based modeling. To best understand how modifying geometric parameters affects the actuation force of our basic mechanism, we designed and fabricated 36 variations using elastic threads, each with one parameter changed while keeping all others identical to the default configuration (Table 1). Table 6 fully lists every permutation. The collected data and the results are illustrated in Figure 11, with shaded areas indicating the range of force over five repetitions of each experiment. Each plot also shows (in gray) the force-displacement curve predicted by the theoretical model (Section 4.2.1).

Our results illustrate that a wide range of forces and displacements are available by changing the values of the geometric parameters of our design for the uniform and flexure frame types. For the thread frame type, using a constant pre-stretch on a single type of elastic thread, forces are only slightly dependent on any of the geometric modifications. Between frame types, higher actuation forces result from uniform, while lower actuation forces come from thread frame types.

In addition, we looked into the robustness of our design by repeatedly activating all three of our default configurations for 1000 cycles and measuring the actuation force after the first and last actuation. For the uniform design, we observed a drop of 5.25%, for the flexure 2.26%, and for the thread 13.72%, with initial base forces of 5.59N, 4.34N, and 0.48N, respectively. We also found that geometric variations can influence robustness: thicker arms, shorter arms, or wider arm separations (resulting in larger horizontal deflection), lead to force values dropping within the first few actuations, suggesting material fatigue (Figure 12(a)).

For the elastic models, the thread pre-stretching is manual, 0.72% pre-stretch corresponds 140mm for the default uniform configuration, but in practice varies. We observe that the stretching can affect the actuation force (Figure 12(b)). To test the accuracy of manual thread-prestretching, we also fabricated eight models in duplicates and with pre-stretched threads: the difference in actuation force was up to 0.53 N. Finally, when comparing the force between the threaded inelastic and elastic models, we observe a maximum difference of 1.79 N. The average difference is 0.4 N (SD: 0.48) for the uniform design and 0.21 N (SD: 0.14) for the flexure designs.

4.3 Post-fabrication Tuning

4.3.1 Experiments. We also tested the impact of our arm-length tuning mechanism. We constructed two tuning frames (Figure 13) with different degrees of flexibility to emulate different possibilities in produced objects. On the more-flexible frame, we tuned one model of each arm type to effective arm lengths of 8, 10, 12, and 17 mm, and on the more-rigid frame, to 12, 16, and 20 mm. We

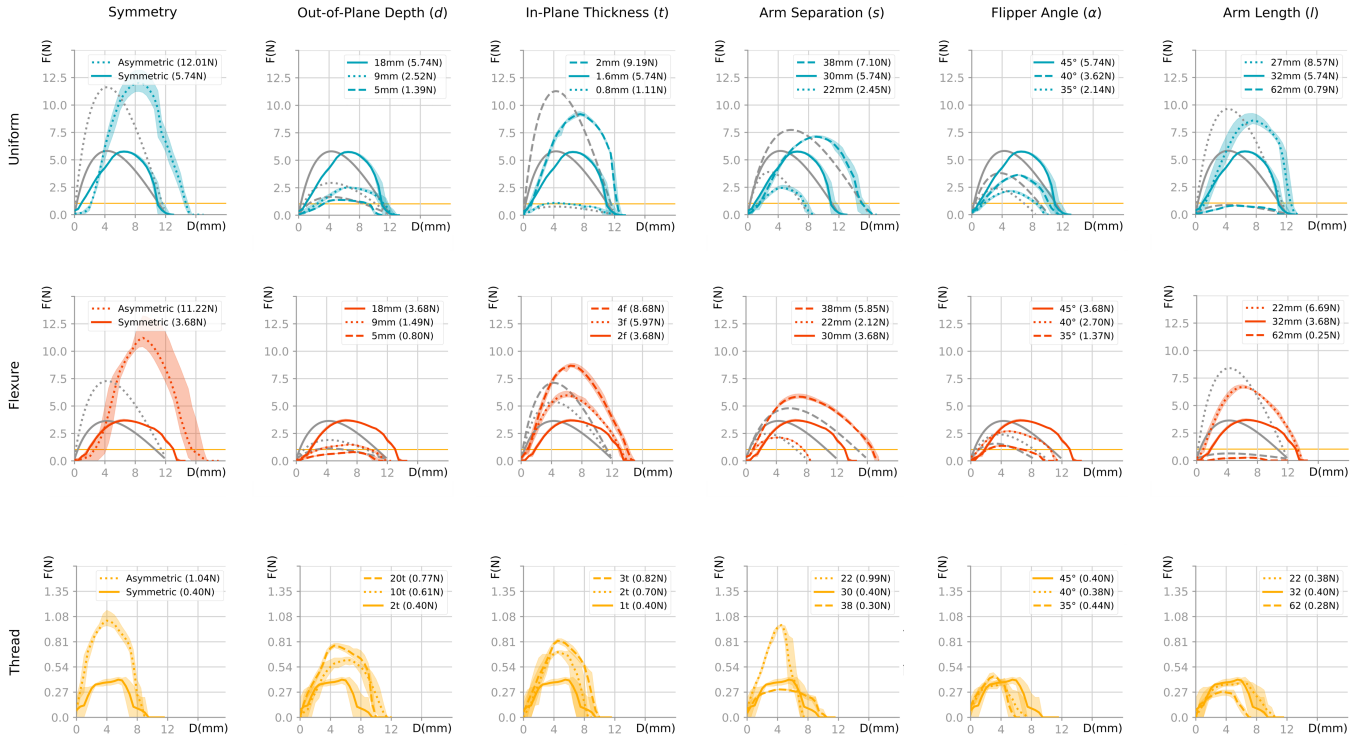


Figure 11: Force-displacement curves for various model parameters. The maximum force before snap-through is written in the legend inside parentheses. The gray lines illustrate our model’s predictions. Note that each row uses a different y -scale, which is shown as a horizontal dashed line on rows with a larger scale.

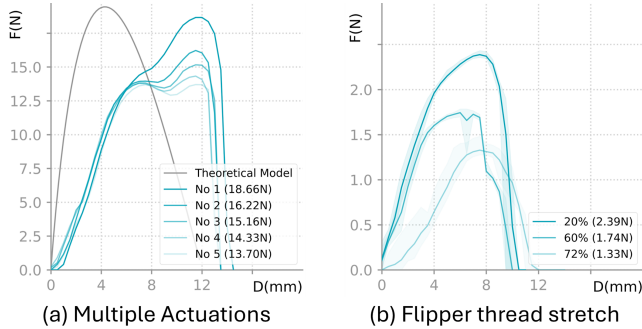


Figure 12: Material fatigue and elastic thread stretch influence force. A model ($t = 2.4$ mm) shows a drop in force after each actuation. A model ($t = 0.8$ mm) shows increasing force as the stretch of the thread increases (b).

recorded the actuation force, repeating five times for each combination. Figure 13 illustrates the results for the uniform and flexure cells.

We found the blocker-based tuning method was not as easy to generalize to the thread cell type, because the blocker becomes a fulcrum around which the arm rotates, causing resistance from the hinge thread rather than the arm itself. This variation led to a very rapid increase in actuation force as the effective arm length

changed (Figure 14(a)). For example, with the rigid frame, we were only able to test at effective arm lengths of 20 and 16 mm before the force became too high for our equipment.

We therefore performed preliminary testing using a thread-stretching-based tuning approach, which gives promisingly stable results (Figure 14(b)). Here, we create tunable resistance via an elastic thread situated across the top of the arms. We tested three different stretch ratios, where a ratio of 1.0 represents that the thread length is equal to the arm distance.

4.3.2 Modeling. We model tuning by fitting the measured force levels to exponential functions of the form $F_u = a(b^\ell) + c$, where ℓ represents the effective arm length and the model parameters a , b , and c for each cell type are found by fitting our recorded data to this model and are shown in Figure 13.

To determine the number of distinctly perceivable force levels suitable for human-operated applications, we reviewed existing literature in haptics [1, 22]. In particular, the lowest achievable force for a design, referred to as the base force F_0 , corresponds to the force experienced when the arms are unrestricted by the tuning mechanism. To compute each subsequent perceptibly distinct force level $F_{i+1}, i \geq 0$, we employ two models. For forces F_i above 2 N, we apply Weber’s law $F_{i+1} = (1+k)F_i$, where the Weber fraction $k = 0.1$ as reported in [1]. For forces below or equal to 2 N we use the model $F_{i+1} = \frac{0.27}{0.33+F_i}$ derived from literature [22]. To determine the placement of the tuning mechanism at effective arm-length ℓ

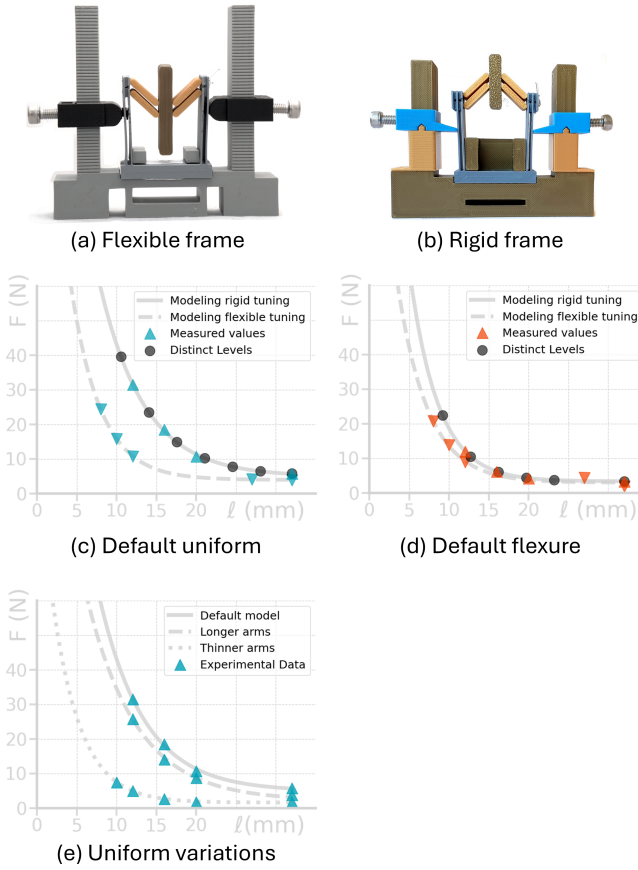


Figure 13: Flexible (Aa) and rigid (b) tuning frames. We measure actuation force (colored marks) at different effective arm lengths ℓ . We fit the measurements to exponential models (gray lines). We calculate perceptible distinct force levels based on Weber’s law (black dots). Results for the default uniform (c) and flexure (d) configurations on the flexible and rigid tuning frames. Comparison between the default uniform and one variation with longer and one with thinner arms (e).

given a desired force level F_u , we use the inverse function:

$$\ell = \frac{\log(\frac{F_u - c}{a})}{\log b}$$

To ensure that the tuning levels (i.e., effective arm lengths ℓ) are easily realized, we recommend a minimum distance of 3.5 mm between them; this limit could be reduced with higher-resolution printers. The black dots on the plots in Figure 13 illustrate several examples of calculated tuning locations and forces. Although in theory, more force levels could be achieved, in practice, the amount of stress and material fatigue imposes limitations. For example, we observe signs of wear for arm length 12 mm in the uniform design at the lower part of the arms, suggesting that shorter arm lengths may not be practically usable using PLA.

For thread-based tuning, we fit the data to a linear function and calculate distinct force levels and stretch ratios accordingly

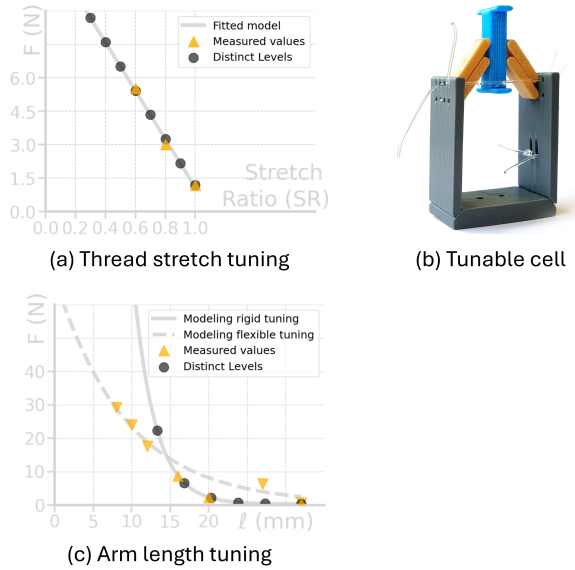


Figure 14: Default thread cell configuration tuned using the arm-length based approach, which gives unstable results (c). Smoother thread-based tuning approach (a); note the elastic thread situated across the tops of the arms (b).

(Figure 14 (b)). The fitted models for all post-fabrication tuning results can be found in the Appendix (Table 5).

5 Design Guidelines

Here we offer guidelines for picking parameters for our bistable mechanism design. Because of variability in 3D printers, printing processes, materials, and fatigue behavior, these guidelines should be viewed as a starting point; experimentation will be required to achieve exactly the desired results.

There are two ways in which the mechanism behavior can be tuned: by making decisions about geometry parameters at design time, pre-fabrication, and by tuning the mechanism post-fabrication.

5.1 Pre-fabrication Tuning

There are many possible combinations of parameters that can affect the operation of the mechanism. To simplify the design process, we recommend that the designer first consider the overall size of the mechanism. A rough rectangular area in which the mechanism should be placed can provide starting values for the arm separation s and arm length l . Next, decide on a vertical displacement D_{ue} from the stable “up” position to the approximate point of snap-through: this can be viewed as the amount of “travel” in the mechanism. Given these values, and a starting default flipper angle α of 45°, subsequent values along with the values for shuttle width w_s and flipper length l_f can be calculated according to equations in Table 2.

The remaining free variables are the arm in-plane thickness t and out-of-plane depth d . Figure 11 illustrates how these values impact the force a user will experience when actuating the mechanism. The force varies with shuttle displacement, and the maximum force

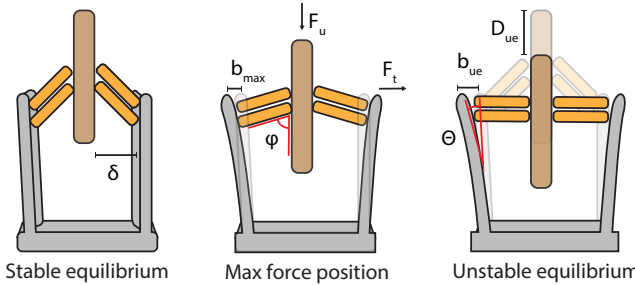


Figure 15: We calculate how much force the flipper (F_t) and subsequently a user (F_u) exerts at a given shuttle displacement based on the horizontal deflection of the arm's tip (b) at this location.

occurs before the snap-through location. Thus, we calculate the maximum user force F_u via several calculations (Appendix B). First, we find the deflection at the point of maximum force, b_{max} :

$$b_{max} = \sqrt[3]{\delta} \cdot \sqrt[3]{l_f^2 - \delta}$$

where δ is the distance between the inner side of one arm and the shuttle (Table 2). We then calculate the angle ϕ_{max} between the flipper and the shuttle:

$$\phi_{max} = \arcsin \left(\frac{b_{max} + \delta}{l_f} \right)$$

We use arm in-plane thickness t and out-of-plane depth d to find the moment of inertia I :

$$I = \frac{d \cdot t^3}{12}$$

We use I , arm length l , and the Young's modulus E (Appendix B) to find F_t , the horizontal component of the force exerted on the flipper by the arm:

$$F_t = \frac{3EIb_{max}}{l^3}$$

Then, we find the vertical component of this force F_u , which is the maximum resistance the user will feel from the shuttle (we multiply by 2 for the case of two symmetrical arms):

$$F_u = 2F_t \frac{\cos \phi_{max}}{\sin \phi_{max}}$$

Finally, substituting I and F_t into F_u and simplifying slightly, we can now predict the force that will be experienced by the user for given values of t and d :

$$F_u = \frac{b_{max} dt^3 E}{2l^3 \tan(\phi_{max})}$$

For asymmetric designs, we use a rough estimate of double the value of the corresponding symmetric. If a sufficiently large force cannot be achieved with the uniform frame due to material fatigue, we iterate by adding more flexures, and we opt for the multi-flexure design. We modeled F_u by modifying its formula, in which we multiply by the number of flexures rather than 2 and by the constant c_f .

As discussed earlier, these equations provide a starting point for design; the designer can vary all of the parameters to achieve

Starting parameters	Starting value	Uniform default
Arm separation (s)	Approx. desired width of cell	30 mm
Shuttle displacement (D_{ue})	Travel before snap-through	12 mm
Flipper angle (α)	Use default value	45°
Building-up parameters	How to choose	
Arm length (l)	Approx. desired height of cell	32 mm
Arm in-plane thickness (t)	Section 5.1	1.6 mm
Arm out-of-plane depth (d)	Section 5.1	18 mm
Derived parameters	How to calculate	
Shuttle width (w_s)	Use roughly $s/5$	6 mm
Arm/shuttle separation (δ)	$\frac{1}{2}(s - w_s)$	12 mm
Flipper arm angle (α)	$\arctan \frac{D_{ue}}{\delta}$	45°
Flipper length (l_f)	$\delta / \cos(\alpha)$	16.97 mm
Young's modulus (E)	Constant (Appendix B)	3.21 GPa

Table 2: Summary of geometrical parameters used in estimating base force for pre-fabrication tuning.

desired effects. Fabricating the models in the physical world creates several limitations. We found that flipper angles α less than 35° led to less-pronounced haptic effects, so recommend $35^\circ \leq \alpha \leq 45^\circ$. The horizontal arm deflection is maximum when the flippers are horizontal and is equal to $l_f - \delta$; based on our experiments, to avoid failure from material fatigue in the arms, we recommend keeping the following two thresholds: $b_{ue} < l/6$ mm and $t < l/18$ mm will help avoid fatigue. To simplify printing, we adjust t to a multiple of our printer's extrusion width (e.g., 0.4 mm).

5.2 Post-fabrication Tuning

As our experimental results show (Section 4.3), blocker-based post-fabrication tuning is influenced by the blocker position (which changes the effective arm length), the space between the blocker and the arm, and the rigidity of the tuning frame. In practice, tuning to exact force levels requires experimentation. As Figure 13 illustrates, the flexibility of the tuning blocker's support influences the uniform cell more than the flexure cell, while a different approach should be considered for the thread cell (Figure 14). If only relative differences are required, the base force F_0 can be estimated (Section 5.1) or measured, and the effective arm length l_i for each successive distinct force level can be computed via

$$l_i = \frac{\log \left(\frac{F_i(k+1)-c}{a} \right)}{\log(b)}$$

with k as described in Section 4.3.2. For identifying values for a , b , c , a designer can print models with a few different arm lengths, measure the actuation force of each, and fit the exponential curve as described in Section 4.3.2.

6 Applications

Bistable cells can be used to move between two stable positions displaying bistability, or to release energy, moving between the unstable equilibrium and a stable position displaying monostability and acting as springs. We explore both functions in our applications as we demonstrate various design and tuning possibilities of our mechanisms, which work as interaction components or as sensors, at many different sizes and force levels, and in multi-mechanism

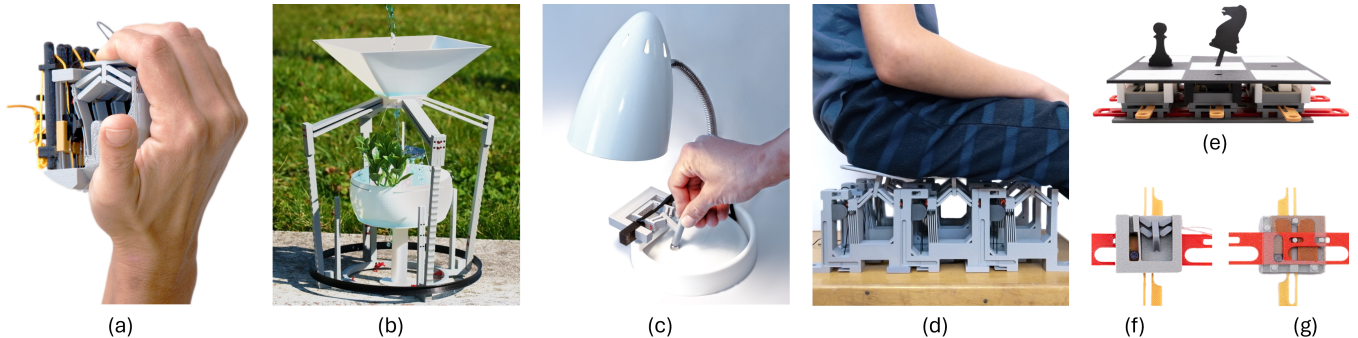


Figure 16: A tunable-force grip strength trainer that can be uniformly tuned (a), a plant house which can deliver a tunable, specific amount of water to a plant (b), a light switch that helps support users' energy consciousness (c), a chair cushion that can be tuned uniformly across its rows (d), and a chess training board that supplies haptic hints about moves (e). The board uses logic gates (f) to selectively tune squares (g). The red sliders enable or disable tuning of each row by shifting a pin left or right. The yellow sliders tune all enabled squares in a column.

configurations of varying complexity. The on-the-spot tuning allows for easy reconfiguration of the actuation force in all examples. We list the design parameters for each application in Table 3, since they were designed earlier than our tuning models.

6.1 Grip Trainer

This hand-scale device has four linearly arranged, individually tunable monostable cells to help people train their grip strength (Figure 16(a))). Unlike most off-the-shelf grip strength trainers, this one provides adjustable actuation forces per finger at multiple levels (see Figure 7, Section 3.2).

6.2 Plant House

A “plant house” that controls irrigation using a large-scale printed bistable mechanism with four arms and a rigid tuning mechanism (Figure 16(b))). When the combined weight of the plant and water in the suspended bucket reaches the desired threshold, the mechanical roof snaps down and blocks further water flow to the plant. Modifying the actuation force level of the roof by sliding the black tuning ring up or down will adjust how much water the plant receives; in this case, the tunable mechanism behaves as a sensor for water quantity. Different force levels provide different water supplies, which can reflect differences in irrigation requirements for different plants or different growth periods [5].

6.3 Light Switch

An adjustable light switch helps users be more mindful of their energy usage; it can be manually set to be easier to switch off and harder to switch on when energy costs are higher (Figure 16(c)). The mechanism attaches to an existing table lamp, with arm and flipper lengths set to match the travel between the existing device's two stable positions. The actuation force of the switch is tunable in discrete levels by adjusting the position of the black blocker. The two different force levels—3.9 N and 4.8 N—are easily discernible, both by the Weber fraction [1] and our experience.

6.4 Chair cushion

Our tunable chair cushion features a 3×3 grid of monostable cells whose resistance can be adjusted per row (Figure 16(d)). Each cell requires a high enough resistance to hold a human's body weight; for these, we use an asymmetric design with five flexures of 1.6 mm each and an out-of-plane depth of 22 mm. Our standard threads were too weak to allow bistable functionality at high force levels, so we threaded the mechanisms using TPU printer filament. Using a force tester with a maximum force capacity of 500 N, we tested the actuation force required to toggle the platform of one cell of our design at different tuning values: we found a range of 43–226 N (4.4–23.0 kg). Across all 9 cells, this means our design can respond to 387–2034 N (39.5–207.4 kg), which corresponds to a wide range of human body weights.

6.5 Chess Instructor

We built a 3×3 grid of bistable mechanisms that support learning chess: using mechanical logic gates and linear tuning in concert, we can help a player understand which moves are allowed, illegal, or poor choices (Figure 16(e)–(g)). Each square on the board has an identical adjustable mechanism positioned underneath it. Despite its small size, the cell remains robust. Inspired by the Zuse Z1 mechanical computer [37] and a 3D printed reconstruction of its logic gates [24], each cell can be individually addressed and tuned by pulling the red and yellow sliders (Figure 16(f), (g) and Figure 8). When an individual square is tuned to the highest actuation force level, the mechanism resists the pin attached to a chess piece enough to prevent its being pressed into the board (knight, Figure 16(e)); a medium actuation force leads to a distinct feeling of resistance, indicating a poor move.

7 Discussion

7.1 Design Modifications

We examined the effects of pre-fabrication geometry choices and post-fabrication tuning on the actuation force of our mechanisms, and in two of our applications, we make the mechanisms behave as monostable springs instead of bistable lockers. Future work could

Type	Chess Fig.16(e)	Switch Fig.16(c)	Gripper Fig.16(a)	Chair Fig.16(d)	Plant Fig.16(b)
Symmetry	Uniform	Thread	Flexures	Flexures	Thread
α	No	Yes	No	No	Yes
s	34°	35°	49°	43°	35°
t	15 mm	30 mm	30 mm	50 mm	186 mm
d	1 mm	1t	2f	5f	2t
l	6 mm	2t	12 mm	22 mm	2t
unit	-	0.8 mm	0.8 mm	1.6 mm	1.75 mm

Table 3: Design parameters for the applications. The unit row indicates the thickness of the unit thread or flexure.

examine other methods of transitioning between monostable and bistable functionality to further expand the range of functional possibilities. Mechanisms that modify the shuttle motion range on the fly could be modeled using threads or rigid body parts. I can add this sentence there Exploring the extension of our technique to multistable mechanisms, or bistable mechanisms with multiple arms (such as the one in our plant house) is also an intriguing possibility suggesting even richer on-the-spot versatility: this could enable reduction of “wobbling” we experienced, where the shuttle did not move perfectly linearly, or even allow designers to intentionally configure a particular non-linear trajectory for shuttles to take.

7.2 Limitations

We printed functional, tunable bistable mechanisms as small as 15 mm and as large as 186 mm. These dimensions were limited by our FFF printers: we could not print objects larger than the print bed, and smaller components were too fragile for our applications. Printing mechanisms larger than the bed size is potentially possible by leveraging techniques similar to TrussFab [23], where only certain pieces are printed while the remainder are appropriated, and smaller mechanisms could be possible with higher-resolution printing processes such as stereolithography (SLA).

All of our mechanisms were hand-threaded after printing, but future work could use thread-embedding printers [3]. A more fundamental limitation relates to the friction on tuning strings when they are used for multiple mechanisms in a sequence: this was not an issue in assemblies at the scale of our applications, but for arbitrary placement of many tunable mechanisms in objects, it will be a consideration. This capstan effect could be mitigated through the inclusion of pulleys in future designs.

The pseudo-rigid-body model captured some of the differences between our mechanism designs, but not all of them. This may be related to their hand-assembled nature or to printing inconsistencies introduced through slicing and the FFF process. We also hope to model our asymmetric, flexure, pre-stretching more fully using elastic threads and hinged frames in the future: these models would depend upon having precise characterizations of the thread used. We also noted that, at rest, the shuttles on low-stiffness designs suffered vertical displacement due to gravity, which could account for discrepancies between the experimental force-displacement curves

and the theoretical model. We also want to investigate the longer-term durability of our mechanisms, especially their threaded parts: this is left as future work.

While we have extensively characterized our mechanism and highlighted some of its possible applications, we believe that its feedback is more complex than our tests could capture. While we presented force-displacement curves according to common practice in the literature, during informal testing we noted that our colleagues did not always perceive mechanism responses in the same way they are numerically characterized: future work could investigate the relationships between maximum force, travel distance, work (in the physics sense), contact area, acoustic features, and perceived haptics [27].

7.3 Future Application Areas

Our applications cells ranged between roughly 23 mm × 33 mm × 6 mm and 200 mm × 267 mm × 200 mm: sizes suitable for finger- (e.g., chess tutor), hand- (e.g., hand gripper), and body-scale (e.g., cushion chair) functional devices. We were earlier able to fabricate cells 10 mm × 13 mm × 4 mm ([33]Fig. 3). These cells, and smaller ones enabled by future fabrication technologies, could enable wide-ranging applications, from comfortable, wearable garments with locally-tunable body supports, to soft robots capable of temporarily hardening or softening on demand, to reconfigurable palpation training devices for subsurface tumor detection [10].

The ability to adjust device haptics according to personal requirements could enable the creation of customizable objects tailored to individual needs and preferences. For example, keyboard buttons could be designed with specific motion and force-feedback profiles based on a user’s physical capabilities, such as limited strength or range of motion. Simple, scalable, tunable, haptic feedback mechanisms could also convey accessible semantic information through force levels: for example, a privacy-preserving ATM interface for blind and low vision users could communicate financial information through reconfigurable, on-screen tactile cues, which are more difficult to intercept than audio information.

8 Conclusion

We have presented a mechanism that provides tunable actuation forces when users interact with it: these forces and the overall behaviour of the mechanism can be tuned pre-fabrication or post-fabrication, as we showed through our experimental and modeling results. We demonstrated various methods to include multiple tunable mechanisms in objects, and to tune them selectively or together. Finally, we illustrated several use cases for pre- and post-fabrication tuning in functional objects through demo applications. Given the accessibility of our mechanism design (which requires only a hobbyist-grade 3D printer, common filaments, and off-the-shelf threads), we hope our readers will “stay tuned” as HCI researchers and makers move towards a rich future of low-cost objects with customizable mechanical properties.

Acknowledgments

We thank the anonymous reviewers for their feedback; Kellie Anne Dunn, Vivien Francis, and Emily Whiting for bringing into our attention research on bistable mechanisms and thread reconfiguration;

Robert Kovacs for sharing his insights on the design and fabrication on bistable mechanisms; Anca-Simona Horvath, Bhaskar Dutt, and Christos Panotopoulos for discussing their ideas about applications of this work; and Liam Ashbrook and Theodosia for serving as models in the chair-cushion photoshoot.

This work was primarily funded by the VILLUM FONDEN under grant number 41007, and partially supported by a Novo Nordisk Fonden Starting Grant under grant number NNF21OC0072716.

References

- [1] S. Allin, Y. Matsuoka, and R. Klatzky. 2002. Measuring just noticeable differences for haptic force feedback: implications for rehabilitation. In *Proceedings 10th Symposium on Haptic Interfaces for Virtual Environment and Teleoperator Systems. HAPTICS 2002*. IEEE Computer Society, USA, 299–302. <https://doi.org/10.1109/HAPTIC.2002.998972>
- [2] Davide Jose Nogueira Amorim, Troy Nachtigall, and Miguel Bruns Alonso. 2019. Exploring mechanical meta-material structures through personalised shoe sole design. In *Proceedings of the 3rd Annual ACM Symposium on Computational Fabrication* (Pittsburgh, Pennsylvania) (SCF '19). Association for Computing Machinery, New York, NY, USA, Article 2, 8 pages. <https://doi.org/10.1145/3328939.3329001>
- [3] Daniel Ashbrook, Wei-Ju Lin, Nicholas Bentley, Diana Soponar, Zeyu Yan, Valkyrie Savage, Lung-Pan Cheng, Huaishu Peng, and Hyunyoung Kim. 2024. Rhapsō: Automatically Embedding Fiber Materials into 3D Prints for Enhanced Interactivity. In *Proceedings of the 37th Annual ACM Symposium on User Interface Software and Technology* (Pittsburgh, PA, USA) (UIST '24). Association for Computing Machinery, New York, NY, USA, Article 120, 20 pages. <https://doi.org/10.1145/3654777.3676468>
- [4] Rafael Ballagas, Sarthak Ghosh, and James A Landay. 2018. The Design Space of 3D Printable Interactivity. *Proceedings of the ACM on Interactive, Mobile, Wearable and Ubiquitous Technologies* 2, 2 (July 2018), 61–21. <https://doi.org/10.1145/3214264>
- [5] C Brouwer and M Heibloem. 1986. Irrigation water management: irrigation water needs. *Training manual* 3 (1986), 1–5.
- [6] Zekun Chang, Tung D. Ta, Koya Narumi, Heeju Kim, Fuminori Okuya, Dongchi Li, Kunihiro Kato, Jie Qi, Yoshinobu Miyamoto, Kazuya Saito, and Yoshihiro Kawahara. 2020. Kirigami Haptic Swatches: Design Methods for Cut-and-Fold Haptic Feedback Mechanisms. In *Proceedings of the 2020 CHI Conference on Human Factors in Computing Systems* (CHI '20). Association for Computing Machinery, New York, NY, USA, 1–12. <https://doi.org/10.1145/3313831.3376655>
- [7] Elaine Chen and Beth Marcus. 1998. Force feedback for surgical simulation. *Proc. IEEE* 86, 3 (1998), 524–530. <https://doi.org/10.1109/5.662877>
- [8] Tian Chen, Jochen Mueller, and Kristina Shea. 2016. Design and Fabrication of a Bistable Unit Actuator with Multi-Material Additive Manufacturing. In *Solid Freeform Fabrication 2016: Proceedings of the 26th Annual International Solid Freeform Fabrication Symposium – An Additive Manufacturing Conference*. <http://hdl.handle.net/20.500.11850/119571>
- [9] Tian Chen, Mark Paulty, and Pedro Reis. 2021. A reprogrammable mechanical metamaterial with stable memory. *Nature* 589 (01 2021), 386–390. <https://doi.org/10.1038/s41586-020-03123-5>
- [10] Michael Dinsmore, Noshir Langrana, Grigore Burdea, and Jumoke Ladeji. 1997. Virtual Reality Training Simulation for Palpation of Subsurface Tumors. In *Proceedings of the 1997 Virtual Reality Annual International Symposium (VRAIS '97)* (VRAIS '97). IEEE Computer Society, USA, 54. <https://doi.org/10.1109/VRAIS.1997.583044>
- [11] Maas Goudswaard, Abel Abraham, Bruna Goveia da Rocha, Kristina Andersen, and Rong-Hao Liang. 2020. FabriClick: Interweaving Pushbuttons into Fabrics Using 3D Printing and Digital Embroidery. In *Proceedings of the 2020 ACM Designing Interactive Systems Conference (DIS '20)*. Association for Computing Machinery, New York, NY, USA, 379–393. <https://doi.org/10.1145/3357236.3395569>
- [12] Ben Greenspan, Eric Gallo, and Andreea Danilescu. 2022. FlexKeys: Rapidly Customizable 3D Printed Tactile Input Devices with No Assembly Required. *Additive Manufacturing, Modeling Systems and 3D Prototyping* (2022), 37. <https://doi.org/10.54941/ahfe1001587>
- [13] Christian Hafner, Mickael Ly, and Chris Wojtan. 2024. Spin-It Faster: Quadrics Solve All Topology Optimization Problems That Depend Only On Mass Moments. *ACM Trans. Graph.* 43, 4, Article 78 (July 2024), 13 pages. <https://doi.org/10.1145/3658194>
- [14] Vincent Hayward, Oliver R. Astley, Manuel Cruz-Hernandez, Danny Grant, and Gabriel Robles-De-La-Torre. 2004. Haptic interfaces and devices. *Sensor Review* 24, 1 (Jan. 2004), 16–29. <https://doi.org/10.1108/02602280410515770> Publisher: Emerald Group Publishing Limited.
- [15] Liang He, Huaishu Peng, Michelle Lin, Ravikanth Konjeti, François Guimbretière, and Jon E. Froehlich. 2019. Ondulé: Designing and Controlling 3D Printable Springs. In *Proceedings of the 32nd Annual ACM Symposium on User Interface Software and Technology (UIST '19)*. ACM, New York, NY, USA, 739–750. <https://doi.org/10.1145/3332165.3347951> event-place: New Orleans, LA, USA.
- [16] Larry L Howell. 2001. *Compliant mechanisms*. John Wiley&Sons, Inc. 135–217 pages.
- [17] Larry L. Howell, Spencer P. Magleby, and Brian Mark Olsen. 2013. *Handbook of compliant mechanisms*. John Wiley & Sons, Inc, Chichester, West Sussex, United Kingdom Hoboken, New Jersey.
- [18] Alexandra Ion, Robert Kovacs, Oliver S Schneider, Pedro Lopes, and Patrick Baudisch. 2018. Metamaterial Textures. In *CHI '18: Proceedings of the 36th Annual ACM Conference on Human Factors in Computing Systems*. ACM, New York, New York, USA, 336–12. <https://doi.org/10.1145/3173574.3173910>
- [19] Alexandra Ion, Ludwig Wall, Robert Kovacs, and Patrick Baudisch. 2017. Digital Mechanical Metamaterials. In *Proceedings of the 2017 CHI Conference on Human Factors in Computing Systems* (Denver, Colorado, USA) (CHI '17). Association for Computing Machinery, New York, NY, USA, 977–988. <https://doi.org/10.1145/3025453.3025624>
- [20] Yu Jiang, Shobhit Aggarwal, Zhipeng Li, Yuanchun Shi, and Alexandra Ion. 2023. Reprogrammable Digital Metamaterials for Interactive Devices. In *Proceedings of the 36th Annual ACM Symposium on User Interface Software and Technology* (San Francisco, CA, USA) (UIST '23). Association for Computing Machinery, New York, NY, USA, Article 56, 15 pages. <https://doi.org/10.1145/3586183.3606752>
- [21] Yuhui Jin, Isabel Qamar, Michael Wessely, Aradhana Adhikari, Katarina Bulovic, Parinya Punpongsonan, and Stefanie Mueller. 2019. Photo-Chromeleon: Re-Programmable Multi-Color Textures Using Photochromic Dyes. In *Proceedings of the 32nd Annual ACM Symposium on User Interface Software and Technology* (New Orleans, LA, USA) (UIST '19). Association for Computing Machinery, New York, NY, USA, 701–712. <https://doi.org/10.1145/3332165.3347905>
- [22] Faezeh Heydari Khabbaz, Andrew Goldenberg, and James Drake. 2016. Force Discrimination Ability of the Human Hand near Absolute Threshold for the Design of Force Feedback Systems in Teleoperations. *Presence* 25, 1 (2016), 47–60. https://doi.org/10.1162/PRES_a_00245
- [23] Robert Kovacs, Anna Seufert, Ludwig Wall, Hsiang-Ting Chen, Florian Meinel, Willi Müller, Sijing You, Maximilian Brehm, Jonathan Striebel, Yannis Kommana, Alexander Popiak, Thomas Bläsius, and Patrick Baudisch. 2017. TrussFab: Fabricating Sturdy Large-Scale Structures on Desktop 3D Printers. In *Proceedings of the 2017 CHI Conference on Human Factors in Computing Systems* (Denver, Colorado, USA) (CHI '17). Association for Computing Machinery, New York, NY, USA, 2606–2616. <https://doi.org/10.1145/3025453.3026016>
- [24] F. J. Krann. 2020. Basic Information and 3D-reconstructions of Zuse's Mechanical Memory and Logic Elements from the Z1 Programmable Calculator. <https://electricrycky.nl/mechanics/zuseGates/>.
- [25] P. R. Kuppens, M. A. Bessa, J. L. Herder, and J. B. Hopkins. 2021. Compliant Mechanisms That Use Static Balancing to Achieve Dramatically Different States of Stiffness. *Journal of Mechanisms and Robotics* 13, 2 (01 2021), 021010. <https://doi.org/10.1115/1.4049438> arXiv:https://asmadigitalcollection.asme.org/mechanismsrobotics/article-pdf/13/2/021010/6660670/jmr_13_2_021010.pdf
- [26] Yu Li, Juan Montes, Bernhard Thomaszewski, and Stelian Coros. 2022. Programmable Digital Weaves. *IEEE Robotics and Automation Letters* 7, 2 (2022), 2891–2896. <https://doi.org/10.1109/LRA.2022.3145948>
- [27] Yi-Chi Liao, Sunjun Kim, Byungjoo Lee, and Antti Oulasvirta. [n. d.]. Button Simulation and Design via FDVV Models. In *Proceedings of the 2020 CHI Conference on Human Factors in Computing Systems* (New York, NY, USA, 2020-04-23) (CHI '20). Association for Computing Machinery, 1–14. <https://doi.org/10.1145/3313831.3376262>
- [28] Hongnan Lin, Liang He, Fangli Song, Yifan Li, Tingyu Cheng, Clement Zheng, Wei Wang, and Hyunjoo Oh. 2022. FlexHaptics: A Design Method for Passive Haptic Inputs Using Planar Compliant Structures. In *CHI Conference on Human Factors in Computing Systems* (CHI '22). Association for Computing Machinery, New York, NY, USA, 1–13. <https://doi.org/10.1145/3491102.3502113>
- [29] Lin Lu, Andrei Sharf, Haisen Zhao, Yuan Wei, Qingnan Fan, Xuelin Chen, Yann Savoye, Changhe Tu, Daniel Cohen-Or, and Baoquan Chen. 2014. Build-to-last: strength to weight 3D printed objects. *ACM Trans. Graph.* 33, 4, Article 97 (July 2014), 10 pages. <https://doi.org/10.1145/2601097.2601168>
- [30] Yiyue Luo, Junyi Zhu, Kui Wu, Cedric Honnet, Stefanie Mueller, and Wojciech Matusik. 2023. MagKnitie: Machine-knitted Passive and Interactive Haptic Textiles with Integrated Binary Sensing. In *Proceedings of the 36th Annual ACM Symposium on User Interface Software and Technology* (UIST '23). Association for Computing Machinery, New York, NY, USA, 1–13. <https://doi.org/10.1145/3586183.3606765>
- [31] Przemyslaw Musialski, Thomas Auzinger, Michael Birsak, Michael Wimmer, and Leif Kobbelt. 2015. Reduced-order shape optimization using offset surfaces. *ACM Trans. Graph.* 34, 4, Article 102 (July 2015), 9 pages. <https://doi.org/10.1145/2766955>
- [32] Mehmet Ozdemir and Zjenja Doubrovski. 2023. Xpandables: Single-filament Multi-property 3D Printing by Programmable Foaming. In *Extended Abstracts of the 2023 CHI Conference on Human Factors in Computing Systems* (Hamburg, Germany) (CHI EA '23). Association for Computing Machinery, New York, NY, USA, Article 1, 1–12. <https://doi.org/10.1145/3544025.3544031>

- USA, Article 323, 7 pages. <https://doi.org/10.1145/3544549.3585731>
- [33] Athina Panotopoulou, Valkyrie Savage, and Daniel Lee Ashbrook. 2024. Threa-D Printing Tunable Bistable Mechanisms. In *Adjunct Proceedings of the 9th ACM Symposium on Computational Fabrication (Aarhus, Denmark) (SCF Adjunct '24)*. Association for Computing Machinery, New York, NY, USA, Article 16, 3 pages. <https://doi.org/10.1145/3665662.3673272>
- [34] J. Qiu, J.H. Lang, and A.H. Slocum. 2001. A centrally-clamped parallel-beam bistable MEMS mechanism. In *Technical Digest. MEMS 2001. 14th IEEE International Conference on Micro Electro Mechanical Systems (Cat. No.01CH37090)*. IEEE, Interlaken, Switzerland, 353–356. <https://doi.org/10.1109/MEMSYS.2001.906551>
- [35] Jin Qiu, Jeffrey H. Lang, and Alexander H. Slocum. 2004. A curved-beam bistable mechanism. *Journal of Microelectromechanical Systems* 13, 2 (2004), 137–146. <https://doi.org/10.1109/JMEMS.2004.825308>
- [36] Jordan R. Raney, Neel Nadkarni, Chiara Daraio, Dennis M. Kochmann, Jennifer A. Lewis, and Katia Bertoldi. 2016. Stable Propagation of Mechanical Signals in Soft Media Using Stored Elastic Energy. *Proceedings of the National Academy of Sciences* 113, 35 (Aug. 2016), 9722–9727. <https://doi.org/10.1073/pnas.1604838113>
- [37] Raul Rojas. 2016. The Design Principles of Konrad Zuse's Mechanical Computers. [https://doi.org/10.48550/arXiv.1603.02396 \[cs\]](https://doi.org/10.48550/arXiv.1603.02396)
- [38] Grégory Savioz, Miroslav Markovic, and Yves Perriard. 2011. Towards multi-finger haptic devices: A computer keyboard with adjustable force feedback. In *2011 International Conference on Electrical Machines and Systems*. IEEE, Beijing, China, 1–6. <https://doi.org/10.1109/ICEMS.2011.6073855>
- [39] T. Schioler and S. Pellegrino. 2007. Space Frames with Multiple Stable Configurations. *AIAA Journal* 45, 7 (2007), 1740–1747. <https://doi.org/10.2514/1.16825>
- [40] Mike Sinclair, Eyal Ofek, Mar Gonzalez-Franco, and Christian Holz. 2019. CapstanCrunch: A Haptic VR Controller with User-supplied Force Feedback. In *Proceedings of the 32nd Annual ACM Symposium on User Interface Software and Technology (New Orleans, LA, USA) (UIST '19)*. Association for Computing Machinery, New York, NY, USA, 815–829. <https://doi.org/10.1145/3332165.3347891>
- [41] Haichuan Song, Jonàs Martínez, Pierre Bedell, Noémie Vennin, and Sylvain Lefebvre. 2019. Colored Fused Filament Fabrication. 38, 5, Article 141 (June 2019), 11 pages. <https://doi.org/10.1145/3183793>
- [42] Aaron Stapel and Just L. Herder. 2004. Feasibility Study of a Fully Compliant Statically Balanced Laparoscopic Grasper. In *International Design Engineering Technical Conferences and Computers and Information in Engineering Conference*, Vol. Volume 2: 28th Biennial Mechanisms and Robotics Conference, Parts A and B, 635–643. <https://doi.org/10.1115/DETC2004-57242>
- [43] Xiaojun Tan, Shuai Chen, Bing Wang, Jie Tang, Lianchao Wang, Shaowei Zhu, Kaili Yao, and Peifei Xu. 2020. Real-time tunable negative stiffness mechanical metamaterial. *Extreme Mechanics Letters* 41 (2020), 100990. <https://doi.org/10.1016/j.eml.2020.100990>
- [44] Yutaka Tokuda and Tatsuya Kobayashi. 2023. Stiff-switch: Finite Stiffness Control Method Using a Thermo-Mechanical Structure and a Low-voltage Pinpoint Heater. In *CHI EA '23 (Hamburg, Germany)*. Association for Computing Machinery, New York, NY, USA, Article 262, 8 pages. <https://doi.org/10.1145/3544549.3585618>
- [45] Jo Vermeulen, Kris Luyten, Elise Van Den Hoven, and Karin Coninx. 2013. Crossing the bridge over Norman's Gulf of Execution: revealing feedforward's true identity. In *CHI '13: proceedings of the SIGCHI conference on human factors in computing systems*. ACM, New York, New York, USA. <https://doi.org/10.1145/2470654.2466255>
- [46] Wenzhong Yan, Talmage Jones, Christopher L. Jawetz, Ryan H. Lee, Jonathan B. Hopkins, and Ankur Mehta. 2024. Self-deployable contracting-cord metamaterials with tunable mechanical properties. *Materials Horizons* 11, 16 (2024), 3805–3818. <https://doi.org/10.1039/D4MH00584H> Publisher: Royal Society of Chemistry.
- [47] Hang Yang and Li Ma. 2020. 1D to 3D Multi-Stable Architected Materials with Zero Poisson's Ratio and Controllable Thermal Expansion. *Materials & Design* 188 (March 2020), 108430. <https://doi.org/10.1016/j.matdes.2019.108430>
- [48] Willa Yunqi Yang, Yumeng Zhuang, Luke Andre Darcy, Grace Liu, and Alexandra Ion. 2022. Reconfigurable Elastic Metamaterials. In *Proceedings of the 35th Annual ACM Symposium on User Interface Software and Technology (Bend, OR, USA) (UIST '22)*. Association for Computing Machinery, New York, NY, USA, Article 67, 13 pages. <https://doi.org/10.1145/3526113.3545949>
- [49] Kentaro Yasu. 2019. Magnetact: Magnetic-sheet-based Haptic Interfaces for Touch Devices. In *Proceedings of the 2019 CHI Conference on Human Factors in Computing Systems (CHI '19)*. Association for Computing Machinery, New York, NY, USA, 1–8. <https://doi.org/10.1145/3290605.3300470>
- [50] Ran Zhang, Thomas Auzinger, and Bernd Bickel. 2021. Computational Design of Planar Multistable Compliant Structures. *ACM Trans. Graph.* 40, 5, Article 186 (Oct. 2021), 16 pages. <https://doi.org/10.1145/3453477>
- [51] Zeang Zhao, Chao Yuan, Ming Lei, Le Yang, Qiang Zhang, Haosen Chen, H. Jerry Qi, and Daining Fang. 2019. Three-Dimensionally Printed Mechanical Metamaterials With Thermally Tunable Auxetic Behavior. *Physical Review Applied* 11, 4 (April 2019), 044074. <https://doi.org/10.1103/PhysRevApplied.11.044074> Publisher: American Physical Society.

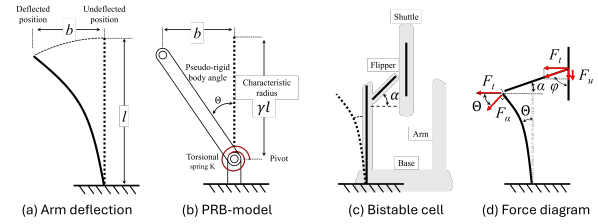


Figure 17: The pseudo-rigid-body model operates on a fixed-free compliant beam with a force at the free end (a, adapted from [17]), which models an equivalent rigid body's rotation (b, adapted from [17]). We can map these values to our uniform frame (c). The forces generated through the user pushing the shuttle, rotating the flippers, and deflecting the arm tip can be represented in a force diagram (d).

- [52] Clement Zheng, Jeeun Kim, Daniel Leithinger, Mark D. Gross, and Ellen Yi-Luen Do. 2019. Mechamagnets: Designing and Fabricating Haptic and Functional Physical Inputs with Embedded Magnets. In *Proceedings of the Thirteenth International Conference on Tangible, Embedded, and Embodied Interaction (TEI '19)*. Association for Computing Machinery, New York, NY, USA, 325–334. <https://doi.org/10.1145/3294109.3295622>
- [53] Clement Zheng, Zhen Zhou Yong, Hongnan Lin, HyunJoo Oh, and Ching Chiu Yan. 2022. Shape-Haptics: Planar & Passive Force Feedback Mechanisms for Physical Interfaces. In *CHI Conference on Human Factors in Computing Systems (CHI '22)*. Association for Computing Machinery, New York, NY, USA, 1–15. <https://doi.org/10.1145/3491102.3501829>
- [54] Shannon A Zirbel, Kyler A Tolman, Brian P Trease, and Larry L Howell. 2016. Bistable mechanisms for space applications. *PloS one* 11, 12 (2016), e0168218. <https://doi.org/10.1371/journal.pone.0168218>
- [55] Ali Zolfagharian, Mohammad Reza Khosravani, and Akif Kaynak. 2020. Fracture Resistance Analysis of 3D-Printed Polymers. *Polymers* 12, 2 (2020), 302. <https://doi.org/10.3390/polym12020302>

A Finite Element Analysis Setup

A finite element analysis was performed using Autodesk Fusion to evaluate the stress distribution in monolithic designs (uniform and flexure-type frames). The model consisted of one arm with its base, as the stresses in the other arm would be similar. The material assigned to the models was PLA, with a Young's modulus of 2.45 GPa. A static analysis was conducted, where one end of the arm was fixed at its base, and the other end was displaced by a 5 N force perpendicular to the length of the beam for both types of frames. The simulation revealed that the uniform frame exhibited a maximum stress of 20.44 MPa, while the flexure frame had a maximum stress of 9.19 MPa. Stress contours indicated that the maximum stress occurred near the base of the arm.

B Pseudo-Rigid-Body Models for Monolithic Frames

The force generated by an arm (here treated as a beam), can be estimated by applying the pseudo-rigid-body model; this model approximates compliant elements as rigid bodies [16, 17]. Figure 17 (a), where a torsional spring with spring constant K_Θ assumed to be located at the endpoint of a rigid body of length $\gamma \times l$ where l is beam length (in our case the arm length). This simplification allows us to determine the required force to rotate at a given angle the equivalent rigid body.

When a user pushes the shuttle, the force they apply is transmitted through the flippers to the arms. This force displaces the shuttle

Symbol	Quantity	Description
E	3.21 GPa	Young's modulus
γ	0.85	Characteristic radius factor of a beam ≤ 1
K_Θ	$\approx \pi \cdot \gamma$	Spring constant
I	$\frac{d \cdot t^3}{12}$	Moment of inertia
δ	$0.5 \cdot (s - w_s)$	Horizontal projection flipper
l_f	$\frac{\delta}{\cos(\alpha)}$	Flipper length
ϕ_0	$\arcsin\left(\frac{\delta}{l_f}\right)$	Flipper shuttle angle at rest (stable) position
D_{ue}	$\cos(\phi_0) \cdot l_f$	Shuttle displacement at unstable equilibrium
b_i	$\sqrt{l_f^2 - (D_u - D_i)^2} - \delta$	Horizontal beam deflection (shuttle at i)
Θ_i	$\arcsin\left(\frac{b_i}{\gamma \cdot l}\right)$	Angle between undeflected and deflected beam (shuttle at i)
α_i	$\arcsin\left(\sin(\alpha) - \frac{D_i}{l_f}\right)$	Angle between flipper and horizontal component (shuttle at i)
ϕ_i	$\arcsin\left(\frac{b_i + \delta}{l_f}\right) = \frac{\pi}{2} - \alpha_i$	Angle between shuttle and flipper (shuttle at i)
F_α	$\frac{K_\Theta \cdot E \cdot I \cdot \Theta_i}{l^2}$	Force perpendicular to the flexure by the pseudo-rigid body model
F_t	$\approx \frac{3 \cdot E \cdot I \cdot b_i}{l^3}$	Horizontal component of the force applied by the flipper
F_u	$2 \cdot F_\alpha \cdot \frac{\sin(\alpha_i)}{\cos(\alpha_i - \Theta_i)}$	Force applied by the user for a arm symmetric design (approach 1)
F_u	$2 \cdot F_t \cdot \frac{\cos(\phi_i)}{\sin(\phi_i)}$	Force applied by the user for 2 arm symmetric design (approach 2)

Table 4: Symbols, quantities, and descriptions used in the pseudo-rigid body model for a given shuttle displacement D_i of a uniform symmetric design and pre-defined geometric parameters, where the beam is the arm in our design.

amount D_i and this result in changes in the angle between the flipper and the horizontal axis to α_i , the angle between the flipper and the vertical axis ϕ_i , the angle Θ_i between the undeflected and deflected beam position, as well as the endpoint horizontal beam deflection b_i .

The required perpendicular to the beam (arm) force F_α for a horizontal deflection of amount b_i can be computed using the formula [16]:

$$F_\alpha = \frac{K_\Theta \cdot E \cdot I \cdot \Theta_i}{l^2}$$

which corresponds to a force perpendicular to the arm. An alternative approach is to quantify the horizontal component (parallel to the base frame) of the force applied by the flipper to the beam F_t [42] for a given deflection b_i , which can be computed by

$$F_t = \frac{3 \cdot E \cdot I \cdot b_i}{l^3}$$

Knowing these forces, we can approximate the user-experienced force F_u for a symmetric two-arm design by finding the vertical component of the force applied by the shuttle to the flipper, and then multiplying by two to account for the two-arm symmetric design. Using the first approach for the shuttle displaced at i , we have:

$$F_u = 2 \cdot F_\alpha \cdot \frac{\sin(\alpha_i)}{\cos(\alpha_i - \Theta_i)} \quad (1)$$

Or alternatively, using the second approach:

$$F_u = 2 \cdot F_t \cdot \frac{\cos(\phi_i)}{\sin(\phi_i)} \quad (2)$$

(Figure 17(b)).

For all of our cells used for modeling forces, we notice that the two formulas provide approximately the same results, if we consider kinematics following the pseudo-rigid body model. In addition, using equation 2 we can directly identify the horizontal arm endpoint deflection for which force is maximized, by finding the real root of its derivative with respect to b :

$$b_{max} = -\delta + \delta^{\frac{1}{3}} \cdot l_f^{\frac{2}{3}} \quad (3)$$

To determine appropriate values for the parameter E , we performed a least squares fitting of the experimental force data to the first approach $F_u + \text{constant}$ (1). The fitting procedure aims to minimize the discrepancy between the maximum experimentally recorded forces, namely, actuation forces, and the modeled user-experienced forces at the horizontal displacement that maximizes force b_{max} for all our inelastic threaded uniform designs. This gave us a value for Young's modulus of 3.21 GPa, and the *constant* to be equal to .07 with a mean squared error corresponding to a force deviation of approximately 102 g, with set γ value of 0.85. To estimate the force in the multi-flexure design, we fit the experimental data to the formula $c_f \cdot F_u$. For the computation of the user-applied

force, we considered each flexure an individual arm. For thickness t we used the thickness of a single flexure. We also updated the user force equation by multiplying it by a constant c_f and replacing the 2 from the earlier two-arm symmetric design formula with the total number of flexures. The constant multiplier value was found to be $c_f = 2.47$. As a crude approximation for the asymmetric design, we doubled the force of the corresponding symmetric design.

C Post-fabrication Tuning

Table 5 shows the model variations and post-fabrication tuning models derived from measuring actuation at a small number of different tuning levels for both tuning approaches. The effective arm length tuning follows exponential functions, while the thread stretching tuning is closer to a linear function. The values of all learned parameters for the designs whose tuning behavior we modeled are presented here.

Frame Type	Variation	Tuning Approach	a	b	c
Uniform	Default	Rigid Frame	226.0	0.8	4.8
Uniform	Default	Flexible Frame	177.8	0.8	3.9
Uniform	Longer arms	Rigid Frame	159.8	0.9	2.1
Uniform	Thinner arms	Rigid Frame	101.8	0.8	1.6
Flexures	Default	Rigid	247.0	0.8	3.3
Flexures	Default	Flexible	144.9	0.8	2.9
Thread	Default	Rigid	2488.1	0.7	0.3
Thread	Default	Flexible	67.9	0.9	0.3
Thread	Default	Stretch-based	-10.9	11.9	-

Table 5: Models derived from post-fabrication tuning. Fitting measured data to exponential models of the form $a \cdot b^\ell + c$ for the arm length tuning or linear models $a \cdot SR + b$ for the thread stretch tuning, where ℓ is the effective arm length and SR the prestretch ratio. Here we present the values for a , b , and c .

D Tested Models and Parameters

Table 6 shows the parameters for the designs we tested. The thickness metric for the thread design is thread count, with thread thickness 0.8 mm. The thickness metric for the flexure design is flexure count with flexure thickness 0.8 mm and in-between gap 1.4 mm.

Arm Type	Symmetry	Flipper angle (α)	Arm length (l)	In-plane arm thickness (t)	Out-of-plane arm depth (d)	Arm separation (s)
	Yes	45°	32 mm	1.6 mm / 2f / 1t	18 mm / 2t	30 mm
Thread	No					
Flexures	No					
Uniform	No					
Thread		35°				
Thread		40°				
Flexures		35°				
Flexures		40°				
Uniform		35°				
Uniform		40°				
Thread			27 mm			
Thread			62 mm			
Flexures			22 mm			
Flexures			62 mm			
Uniform			22 mm			
Uniform			62 mm			
Thread				2t		
Thread				3t		
Flexures				3f		
Flexures				4f		
Uniform				0.8 mm		
Uniform				2.0 mm		
Flexures					9 mm	
Flexures					5 mm	
Uniform					9 mm	
Uniform					5 mm	
Thread					20t	
Thread					10t	
Thread						22 mm
Thread						38 mm
Flexures						22 mm
Flexures						38 mm
Uniform						22 mm
Uniform						38 mm

Table 6: Variations of our cell design. Blank table cells indicate that the defaults shown in the header apply to that variation.